



# Redox cycling of Ni–YSZ anodes for solid oxide fuel cells: Influence of tortuosity, constriction and percolation factors on the effective transport properties



L. Holzer<sup>a,\*</sup>, B. Iwanschitz<sup>b</sup>, Th. Hocker<sup>a</sup>, L. Keller<sup>a</sup>, O. Pecho<sup>a</sup>, G. Sartoris<sup>a</sup>, Ph. Gasser<sup>c</sup>, B. Muench<sup>d</sup>

<sup>a</sup>ZHAW, Zurich University of Applied Sciences, Institute of Computational Physics – ICP, Wildbachstrasse 21, CH-8400 Winterthur, Switzerland

<sup>b</sup>Hexis Ltd, Zum Park 5, CH-8404 Winterthur, Switzerland

<sup>c</sup>ETHZ, Swiss Federal Institute of Technology, EMEZ, Centre for Imaging Science and Technology, CH-8093 Zürich, Switzerland

<sup>d</sup>Empa, Materials Science and Technology, Laboratory for Concrete and Construction Chemistry, Ueberlandstr. 129, CH-8400 Dübendorf, Switzerland

## HIGHLIGHTS

- Redox degradation of Ni–YSZ anode is described by 3D-imaging.
- The effective electrical and ionic conductivities are predicted based on 3D-topology.
- Electronic transport decreases due to changes of percolation and constrictivity in Ni.
- Ionic transport is limited by constrictivity (narrow bottlenecks) in YSZ.

## ARTICLE INFO

### Article history:

Received 1 August 2012

Received in revised form

13 April 2013

Accepted 9 May 2013

Available online 21 May 2013

### Keywords:

FIB-tomography

3D image analysis

Effective transport property

Microstructure degradation

Cermet

## ABSTRACT

A methodology based on FIB-tomography and image analysis (IA) is proposed which allows quantification of all relevant morphological features that are necessary to predict effective transport properties in porous SOFC electrodes. These morphological features are constrictivity, tortuosity, percolation factor and phase volume fraction. An *M*-factor can then be calculated which represents the ratio of effective over intrinsic conductivities. The methodology is used to describe effects of microstructure degradation in Ni–YSZ anodes which are caused by redox cycling at 950 °C. The so calculated *M*-factors predict that because of redox cycling the effective electronic conductivity of nickel decreases from 3 to 1.2% which is mainly due to changes of percolation and constriction factors. Based on these results the effective electrical conductivity of nickel is predicted to be 685 S/cm before redox and 243 S/cm after 8 redox cycles. The predictions fit well with the experimental measurements that reveal 600 S/cm before and 200 S/cm after redox cycling at 950 °C. For YSZ the *M*-factors obtained with 3D-analysis predict that the degradation causes a drop of the effective ionic conductivity from 7 to 0.6%, which is due to a change of the bottleneck dimensions. This finding contradicts the frequent interpretation of YSZ as a 'rigid backbone' that is not affected by microstructure degradation. Finally, the effective bulk gas diffusivity increases from 2 to 11% due to an increase of porosity associated with swelling of the anode.

© 2013 Elsevier B.V. All rights reserved.

## 1. Introduction

Porous Ni–YSZ cermet is a standard anode material for high temperature solid oxide fuel cells (SOFCs). The reaction mechanism of such composite anodes includes a complex interplay of electrochemical reactions (oxidation of fuel at the triple phase

boundary, TPB) with various transport processes (electronic conduction in nickel, ionic transport in YSZ and gas diffusion in the pores). As described by Costamagna et al. [1] the electrode mechanism and associated performance can be simulated with a coupling of the transport processes (solved via ohms law) with the electrochemical reactions (described by Butler–Volmer equation). A major challenge for such simulations is the incorporation of morphological features as for example the effects of variable grain sizes and variable compositions. A first approximation can be done with microstructure models that are based on idealized and

\* Corresponding author. Tel.: +41 58 934 77 90.  
E-mail address: [holz@zhaw.ch](mailto:holz@zhaw.ch) (L. Holzer).

simplified particle shapes. For example, Abbaspour and Kenney [2–4] presented numerical simulations of 3D-microstructures in porous electrodes which consist of spherical particles (Ni and YSZ). It was demonstrated that the simulations with such simplified microstructures are capable to describe the basic relationships between the TPB length with anode composition (Ni/Ni + YSZ) and with particle size. Under the assumption that the TPB length represents the active reaction sites, these numerical models in principle also capture the basic relationships between electrochemical activity with variable compositions or particle sizes. However, if one wants to simulate the electrode mechanism and performance in a realistic way, all relevant properties including the effective transport properties have to be described accurately. In this context it is important to note that the effective transport properties cannot easily be deduced from models with simplified particle shapes. In reality, subtle changes e.g. in the dimensions of the bottlenecks can have a large impact on the effective transport properties, especially for compositions close to the percolation threshold. Therefore the morphological details, which are relevant for the transport properties, can only be captured in an accurate way by using high-resolution 3D-imaging techniques. In this context the recent progress of serial sectioning with focused ion beam (FIB) technique opens new possibilities to study SOFC electrodes. For a review of FIB-tomography (method and applications), which is also called FIB–SEM serial sectioning, see Holzer and Cantoni [5]. Alternatively, the resolution of X-ray tomography has also improved considerably and it is now suitable for the study of electrode microstructures. Both techniques, FIB- and X-ray tomography, were extensively used during the last few years for quantitative analysis of anode microstructures [6–15]. It is important to note that so far most of these 3D-studies on SOFC electrodes mainly intended to quantify electrochemical reaction sites and to distinguish between active and inactive TPBs. Only a limited number of studies were focusing on the relationships between morphological features and transport properties despite the obvious importance of this topic. In this context, two exceptional investigations from the group of Prof. W. Chiu merit to be mentioned:

- a) Grew et al. [16,17] studied the effect of 3D microstructures on the transport phenomena in the YSZ phase of cermet anodes with a lattice Boltzmann method, which provides information about localized resistive losses due to Joule heating. In addition, the 3D microstructures were characterized by phase size distributions, which are obtained with a ray-shooting method. The combination of both techniques opens the possibility to coherently examine the detailed geometry and the associated resistive loss, which finally results in resistive loss distributions (RLDs). The RLD thus links the local resistive losses (Joule heating) with the associated local phase sizes in the microstructure. The RLD measurements document that transport losses mainly originate at locations with small phase sizes. These 'high-loss locations' can be interpreted as constrictions (so-called bottlenecks) in the percolating network of the conducting phase (in this case conduction of oxygen ions in YSZ was considered).
- b) In more recent investigations, Nelson et al. [18,19] developed 1D- and 2D-models (electrochemical fin) to simulate the effect of varying cross-sections along the transport pathways (i.e. constrictions in YSZ). The models are capable of replicating experimentally observed electrode behavior such as the influence of electrode thickness on polarization resistance. Thereby varying cross-sections are described with a sintering quality parameter (SQ). In the modeling framework, a suite of dimensionless parameters (e.g. fin efficiency and base current) and performance metrics (transport resistivity/charge transfer

resistivity) are established. From the correlation between dimensionless parameters and performance metrics, different transport regimes could be identified, which allows performance predictions for different types of microstructures (SQ).

In the above-mentioned investigations [16–19], constrictions and varying cross-sections are identified as important morphological features, which have a considerable influence on the transport properties. In these studies it was emphasized that, in order to establish a link between results from modeling with experimental results from laboratory samples, a method should be developed which allows measuring the constrictivity (i.e. a parameter that describes varying cross-sections and sintering quality) directly from realistic samples with complex disordered microstructures. Under this perspective, our own developments of 3D techniques become important. In a recent paper we have thoroughly described a methodology, which enables to quantify the constrictivity based on data from tomography [20] (a short description is also given below, in Section 2.3.4). In this recent work we have also described further methods for the quantification of additional morphological parameters which are relevant for the transport properties, such as the tortuosity and the percolation factor. Hence a 3D-toolbox was established, which enables describing the most important topological parameters that are relevant for the effective transport properties. The ultimate goal of these developments is the prediction of the effective transport properties entirely based on 3D microstructure analysis (and intrinsic transport properties). For this purpose the quantitative relationships between topological parameters and effective transport properties have to be established empirically. A first empirical study in this direction was performed by Wiedenmann et al. [21], who applied those 3D methods in combination with impedance spectroscopy for the investigation of porous membranes in alkaline electrolysis cells. Thereby the overall impact of the microstructure on the effective ionic diffusivity is described by the so-called *M*-factor, where '*M*' stands for microstructure. The *M*-factor is equivalent to the ratio of the effective ( $\sigma_{\text{eff}}$ ) over the intrinsic transport properties ( $\sigma_0$ ):

$$M = \sigma_{\text{eff}}/\sigma_0 \quad (1)$$

The intrinsic properties ( $\sigma_0$ ) characterize transport in a pure medium (e.g. diffusion in liquid electrolyte or electronic conductivity in pure nickel) without microstructure effect. Based on the experimental results it was shown that the effective transport properties can indeed be described with the *M*-factor, which itself is defined as the product of four distinct microstructure parameters, i.e. phase volume fraction ( $\phi$ ), percolation factor (*P*), constriction factor ( $\beta$ ) and inverse tortuosity ( $1/\tau$ ):

$$M = (\phi P \beta)/\tau \quad (2a)$$

In some publications (e.g. [25]) the effect of tortuosity on the transport properties is described as being proportional to  $1/\tau^2$ :

$$M = (\phi P \beta)/\tau^2 \quad (2b)$$

An open question addressed in the present paper is thus whether the impact of geometric tortuosity on the effective transport properties follows equation (2a) or (2b).

It must be emphasized that equations (1) and (2) were formulated a long time ago based on theoretical and semi-empirical considerations. The relevant 'historical literature' goes back to Kozeny, 1927 [22], Carman, 1956 [23], Archie, 1942 [24], Clennell, 1997 [25], Van Brakel and Heertjes, 1974 [26], and Petersen, 1958 [27]. A thorough discussion of these historical papers about

microstructure effects on transport properties is beyond the scope of the present work, but we have summarized these works in an earlier publication [20]. The synthesis that can be drawn from the historical literature is the formulation of a hypothesis, which states that the effective transport properties can be predicted based on a set of volume-averaged topological parameters, which then leads to equations (1) and (2). For many decades, however, it was impossible to quantify the volume-averaged parameters used in equation (2) because no suitable techniques were available. The recent progress in 3D-imaging and 3D-image analysis now opens new possibilities. Today, all transport relevant parameters can be determined, for example with our 3D-toolbox. These techniques are described below in the methodology section, but more details can be found in the following original papers: Münch and Holzer [28], Keller et al. [29,30] and Holzer et al. [20].

In the present study these 3D techniques are used to characterize microstructure degradation in a Ni–YSZ anode during redox cycling. More specifically we want to investigate how the effective transport properties in nickel, YSZ and pores are affected by redox cycling, and how the measured performance drop relates to changes of the relevant morphological features (i.e.  $\phi$ ,  $P$ ,  $\beta$  and  $\tau$ ).

On a qualitative level, microstructure degradation in nickel cermets which is caused by redox cycling is well described e.g. by Sarantaridis and Atkinson [31], Klemenso and Mogensen [32], Virkar et al. [33] and Fouquet et al. [34]. Their observations of the redox process in Ni based anodes can be summarized as follows: The oxidation of nickel to form nickel oxide is associated with a volume increase of 70%. Due to the expansion of the nickel grains the entire material is ‘swelling’ on a macroscopic scale. The kinetics of the oxidation process is mainly controlled by the diffusion of nickel (outwards) and oxygen (inwards) through the oxidation layer. For temperatures that are typical for SOFC operation (600–1000 °C), the nickel grains become fully oxidized within a relatively short time. For example at 800 °C a 1  $\mu\text{m}$  thick NiO-layer is formed within 4 min. During the re-reduction metallic nickel nuclei are first formed on the surface of the nickel oxide. Reduction leads to a volume decrease so that the surface of the metallic nickel grains remains accessible for the reducing gas and hence the kinetics of this process is controlled by surface reaction instead of diffusion. Subsequently the small nickel grains tend to minimize their surface energy due to the relatively high temperatures, which leads to the formation of larger nickel agglomerates. Thereby nickel is most probably mobilized as a (volatile) metal-hydroxide species, which re-precipitates at preferred locations in the microstructure.

Jeangros et al. [35] performed in situ redox experiments with an environmental TEM. The TEM observations correlate well with their calculations based on density functional theory (DFT). The authors describe that the reduction process of NiO is triggered at the interface with YSZ, where oxygen ions from NiO migrate to the sites of oxygen vacancies in the neighboring YSZ-phase. Thereby nano voids are formed at the NiO–YSZ interface. Also during the oxidation process pore formation is an important feature, which is observed at the interface between metallic Ni and the NiO-layer. This phenomenon is explained by the outward diffusion of Ni.

On a grain scale the volume expansion caused by oxidation can be considered to be reversible during re-reduction. However on a microstructure scale the volume changes are not fully reversible due to the formation of internal porosity (subsequently called pore-swelling). This leads to a macroscopic swelling upon repeated cycling, whereby also the network of the ceramic phase undergoes dilation and the distances between the rigid YSZ grains have to increase. Nevertheless, the YSZ-phase is generally considered as a rigid backbone, which ensures a certain mechanical stability to the cermet material. At this stage a quantitative description of redox induced microstructural changes in cermet anodes is largely

missing. This is particularly true for the allegedly rigid YSZ backbone.

The present work focuses on quantitative microstructure analysis of Ni–YSZ anodes from electrolyte-supported cells. The evolution of the electrical conductivity over eight redox cycles in such anodes was characterized with 4-pt-measurements by Iwanschitz et al. [36]. The conductivity increases from 600 to 650 S/cm after the first redox-cycle at 950 °C. Afterward it gradually decreases to 200 S/cm after 8 redox cycles. Qualitatively it is obvious that these changes are somehow associated with the nickel coarsening that is accelerated upon redox cycling. However it is not clear which morphological parameters in the nickel phase actually control the decrease of the electrical conductivity.

In a similar way also the changes in the YSZ-phase are poorly understood. The ionic conductivity can be measured experimentally by dissolving the nickel phase from the cermet anode and then analyzing the remaining ceramic backbone. In this way, it was shown by Klemenso and Mogensen [32] that the ionic conductivity of YSZ significantly decreases during redox cycling. Under the traditional view that the ceramic phase represents a rigid backbone, which stabilizes the cermet material, the measured drop in ionic conductivity is somewhat surprising. Two explanations are possible: a) the properties of YSZ are changing without any degradation on the grain scale, but only due to a transformation from cubic to tetragonal crystallographic system. Alternatively, it was reported that the particle size of YSZ is changing due to the mobility of Zr-species under SOFC operating conditions [15,37,38], which may explain the measured drop in ionic conductivity. In any case, a change in ionic conductivity may significantly affect the overall performance of the anode and therefore more detailed microstructural investigation is required to understand YSZ degradation upon redox cycling.

In the present study quantitative microstructure analyses are performed for nickel–YSZ samples, which are selected from a previous experimental investigation by Iwanschitz et al. [36]. Two anodes before and after eight redox cycles are compared with each other. Thereby the changes of first order parameters (i.e. volume fractions and size distributions) are documented for all three phases (nickel, YSZ and pores). This enables a quantitative description of nickel coarsening and pore swelling. Based on the 3D-data from FIB-tomography higher order topological parameters (i.e. constriction factor, tortuosity and percolation factor) are extracted. From these parameters the *M*-factors can be calculated according to eq. (2) and the effective transport properties can be predicted according to eq. (1). The data sets from FIB-tomography are then also transformed into grid representations of the corresponding microstructures. These meshed grids are used as a basis for transport simulations by finite element (FE) modeling. As an outcome, the *M*-factors and the effective transport properties obtained by image analysis and by FE-simulations can be compared with the experimentally measured electrical conductivities. In this way a thorough description of the transport relevant parameters can be obtained for all three phases in nickel–YSZ anodes. Furthermore it can be tested whether the *M*-factors obtained by image analysis and by FE-simulation are capable to predict the effective electrical conductivity of a cermet anode and its degradation upon redox cycling.

## 2. Experimental

### 2.1. Anode fabrication, redox experiments and conductivity measurements

Porous anodes are fabricated by screen-printing of Terpeneol-based slurries on a 3YSZ substrate (Nippon Shokubai, 140  $\mu\text{m}$ ).

The slurries are mixed from commercial powders of NiO (J.T. Baker, purity > 99%) and 8YSZ (Mel Chemicals, purity > 99%). The ratio of these powders is chosen so that the solid volume fraction (Ni:8YSZ) after reduction is 40:60 vol%. After screen-printing the anodes are sintered at 1350 °C for 4 h.

For the degradation experiment eight redox cycles are carried out at 950 °C in a tube furnace. The samples are re-oxidized for 30 min. Afterward the re-reduction step is carried out by ramping up the H<sub>2</sub> flow within 5 min and waiting for at least 30 min in order to equilibrate the samples. The redox procedure is repeated eight times.

For the subsequent measurement of electrical conductivity smaller samples of  $8.7 \times 21 \text{ mm}^2$  are cut with a laser from the anode half-cells. 4-point measurements are then performed in an alumina tube at 950 °C (gas flow of 200 N ml/min with 5% H<sub>2</sub> and 95% N<sub>2</sub>). During the conductivity measurements the Nernst potential was constant at 1.1 V. Further details about the sample fabrication, redox-experiments and the corresponding physical and electrochemical characterization are given in Ref. [36].

## 2.2. Image acquisition by SEM and FIB-tomography

For microstructure analysis polished cross-sections are prepared from the samples, which were previously used for conductivity-measurements. For this purpose the pores are impregnated with low viscosity resin (AralditBY158/Aradur21 supplied by Huntsman). Mechanical polishing is performed on textile substrates with diamond suspensions of 6 µm, 3 µm and 1 µm (MetaDi mono-crystalline diamond suspension, Buehler).

For 2D-analysis by scanning electron microscopy (SEM), cross-sections through the anodes are produced with a focused ion beam machine (FIB) from ZEISS (NVision 40). FIB cross sectioning is performed because the results from earlier SEM investigations indicate that conventional mechanical polishing of redox exposed anodes leads to preparation artefacts.

3D-image volumes are acquired by FIB tomography with a Helios Nanolab 600 (DualBeam FIB from FEI). Both FIBs are located at the Electron Microscopy Centre at ETH Zürich (EMEZ). Acquisition of image stacks by FIB tomography includes the following steps: a) Gas assisted metal deposition of a 1 µm thick Pt layer in order to protect the surface from ion milling artefacts. b) Preparation of a cube with dimensions of approximately  $20 \times 20 \times 20 \text{ µm}$  in order to reduce shadowing effects and re-deposition. c) Automated acquisition of an image stack is obtained by repeated and alternating execution of erosion (FIB) and imaging (SEM). The serial sectioning with the ion beam is performed at an acceleration

voltage of 30 kV and a current of 2.5 nA. Electron images are acquired at 2.0 kV, 0.69 nA, in mode 2 with a through-the-lens-detector (TLD). More detailed descriptions of FIB-tomography are given in earlier publications from our group [39–43]. In particular we refer to a recent ‘review of FIB-tomography’ [5].

Fig. 1 represents a comparison of the microstructures in Ni–YSZ anodes before and after redox cycling from FIB/SEM cross-sections (images after segmentation). Qualitatively an increase of porosity and coarsening of the nickel grains can be observed. The size of the image windows and the corresponding pixel/voxel resolutions for the 2D and 3D images are given in Table 1. It is important to note that FIB cross-sections usually provide relatively small image windows, which can be a limitation for representative analyses of disordered microstructures. In earlier investigations on similar cermet anodes as the ones from the present study [11,12] it was shown that representative results are obtained if a cumulated image window size of  $\geq 400 \text{ µm}^2$  is reached. This value is taken as a lower limit in the present study. In order to increase the cumulated window size, the 2D analyses in this study are always averaged over at least two FIB cross-sections from different locations in the same sample. Therefore we are confident that the chosen cumulated window sizes for the 2D analyses give representative results.

For the 3D analyses the image windows are in a similar range as for the 2D cross-section (see Table 1). In fact the PSDs obtained from 2D-cross-sections and from 3D-stacks are nearly identical (see Fig. 4). Since 2D and 3D data for the PSDs in Fig. 4 are collected from different locations in the sample, the coherent PSD results strongly support that all these analyses are representative and reliable.

## 2.3. Image analysis: determination of transport relevant microstructure parameters

First order parameters such as the phase size distribution and the phase volume fractions can be determined based on 2D-images. However, transport relevant parameters (e.g. connectivity) require higher order topological information, which can only be obtained from 3D-images. The most important parameters, which influence the effective transport properties apart from the phase volume fractions, are constrictivity, tortuosity and the percolation factor. The procedures for quantification of these parameters are briefly described in the following sections.

### 2.3.1. Pre-processing: noise filtering, stack alignment, segmentation

Before quantification the image stacks from FIB-tomography have to be pre-processed with the following steps: a) alignment of the stack, b) cropping of a region of interest, c) noise filtering, d)

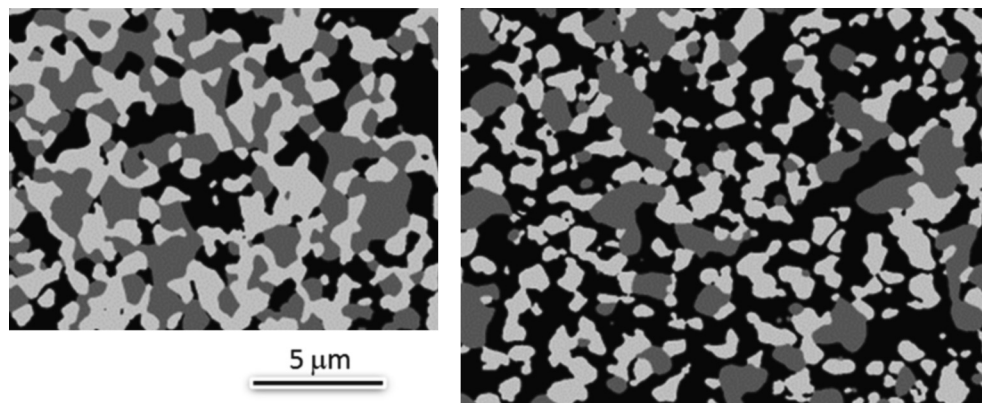


Fig. 1. Segmented SEM images from FIB-cross-sections of Ni–YSZ anodes before (left) and after (right) redox cycling. Note the strong increase of porosity due to redox cycling. Legend: pore (black), nickel (dark gray) and YSZ (bright gray). Both images are at the same magnification (see scale bar).



**Table 1**

Summary of image data (dimensions of image windows and pixel/voxel resolutions in nm) for 2D and 3D analyses of Ni–YSZ anodes before and after redox cycling.

Type of analysis	Redox-cycles	Pixel size (nm)	Pixel matrix		Nr of images	Total nr of pixels/voxels	Size of image window			
			x	y			x	y	z	Total
2D	0	16.00	1024	768	2	1,572,864	16.38	12.29	(2x)	402.65 $\mu\text{m}^2$
3D	0	20.00	995	1304	733	951,052,840	19.90	26.08	14.66	7608.42 $\mu\text{m}^3$
2D	8	19.39	1015	762	2	1,546,860	19.68	14.78	(2x)	581.58 $\mu\text{m}^2$
3D	8	20.00	1171	1343	461	724,993,033	23.42	26.86	9.22	5799.94 $\mu\text{m}^3$

segmentation and e) visualization. For 2D images noise filtering and segmentation is performed with the same tools as for the 3D stacks. For these steps the software packages Fiji (<http://fiji.sc/wiki/index.php/Fiji>) and Avizo (<http://www.vsg3d.com/avizo/overview>) are used. Two 3D reconstructions of image stacks from FIB tomography (after segmentation) are shown in Fig. 2. The comparison shows that redox cycling leads to a significant increase of the pore volume and pronounced coarsening of the nickel phase.

For quantitative analyses of the transport relevant parameters we use homemade software, which was developed with Matlab and Java (see e.g. [28]). The different parameters and the corresponding methods can be described as follows:

### 2.3.2. Continuous phase size distributions (c-PSD) and phase volume fractions ( $\phi$ )

For a quantitative description of nickel coarsening and pore swelling reliable methods for the analysis of object sizes (particles and pores) are required. Conventional methods are based on the size measurement of isolated, discrete objects. However, a major problem for the analysis of discrete phase size distributions (d-PSD) from disordered microstructures is the fact that the pore and solid phases usually form a continuous network. Neither the pore phase nor the sintered solid phases (nickel and YSZ) do consist of discrete objects (i.e. distinct particles or pores). The recognition of discrete objects thus represents a major problem for the statistical description of disordered microstructures with the conventional methods of a 'discrete' phase size distribution. Therefore an alternative procedure of a so-called 'continuous phase size distribution' (c-PSD) was developed by Münch and Holzer [28]. The concept of the continuous PSD is to determine the amount of pore volume (3D) or pore area (2D), which potentially can be covered with

spheres and circles of the radius ( $r_s$ ), in 3D and 2D, respectively. Thereby the entire phase is considered as a continuum. By decreasing the radius ( $r_s$ ) incrementally, increasingly higher volume fractions are covered and in this way a cumulative continuous size distribution is obtained. As shown in Fig. 4 the c-PSD curves of disordered microstructures typically have an even and smooth shape without any significant discontinuities. It is important to note that the 'bulges' (i.e. large pore objects or, alternatively, large particles) contribute with a much larger volume to the c-PSD measurement than regions corresponding to bottlenecks or narrow dead ends. Therefore the so-called  $r_{50}$  value (i.e. the radius corresponding to 50 vol% in the cumulative c-PSD curve) is considered as a statistical measure for the average size of these bulges. Another important aspect is the fact, that the distance map for c-PSD measurement always includes the entire volume of a phase, irrespective of the degree of percolation. Hence, the cumulative c-PSD curve always reveals an analysis over the total phase volume fractions, which are summarized in Fig. 3 for nickel, YSZ and pore in the two investigated samples.

In previous studies the c-PSD method was applied for analyses of different materials (cement, clays, ceramics, and SOFC electrodes). It was observed that the analyses from 2D images and from 3D data volumes show very similar results [44]. Hence, already from 2D-images, the c-PSD method is capable to describe reliably the phase size distributions (e.g. Ni-coarsening) and associated compositional changes (e.g. increase of porosity) [12]. The results of the present study confirm that 2D- and 3D-analyses of c-PSD and phase volume fractions are nearly equivalent (see Fig. 4).

It must be emphasized here that the results from phase size analyses strongly depend on the applied methodology and its underlying geometric definition of 'size', which is not the same for c-

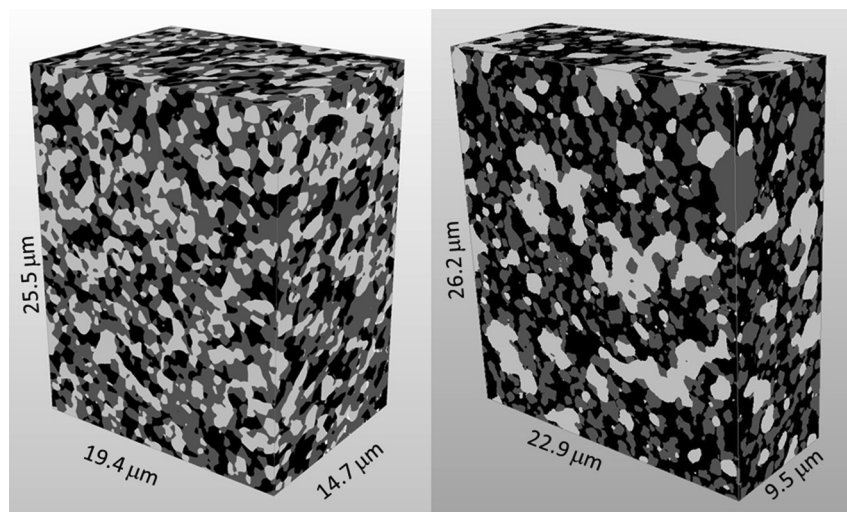


**Fig. 2.** 3D-visualization (FIB-tomography) of Ni–YSZ anodes before (left) and after (right) redox cycling. The initial gray scale images are segmented into pores (black), YSZ (dark gray) and nickel (bright gray).

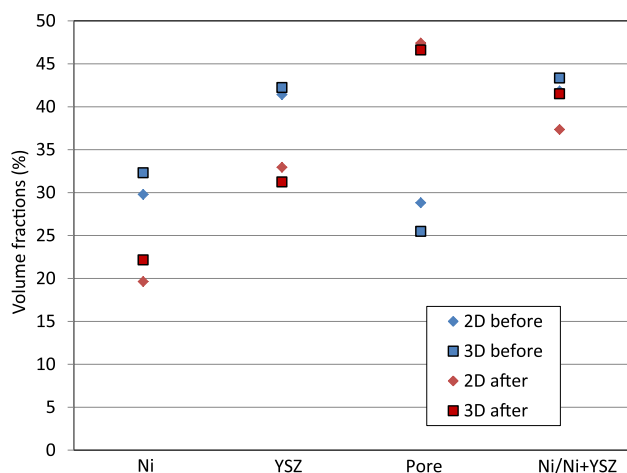


**Fig. 3.** Phase volume fractions of Ni–YSZ anodes before and after 8 redox cycles, measured with image analysis. Redox cycling leads to a significant increase of porosity whereas the ratio of the solid phases ( $\text{Ni}/(\text{Ni} + \text{YSZ})$ ) remains nearly unchanged. 2D and 3D analyses reveal very similar results.

PSD, d-PSD, MIP-PSD, chord distributions and intercept methods. Technical information how these different size distributions are collected can be found in Ref. [28] for c-PSD and MIP-PSD, [41] for d-PSD and [17] for chord distributions based on ray-shooting. For a short discussion about the interpretation of these different PSD types we refer to an earlier publication [12] where we also discuss some advantages and drawbacks of each method (see Fig. 3 in Ref. [12]).

### 2.3.3. Mercury intrusion porosimetry (MIP) and percolation factor ( $P$ )

For the effective transport properties in porous and composite media the dimensions of the bottlenecks and the state of percolation are of great importance. In this context mercury intrusion porosimetry (MIP) provides interesting information. During MIP experiments, the mercury is pressed into the porous sample by incrementally increasing the liquid pressure. According to the Washburn equation an inverse relationship exists between the applied pressure and the radius of the meniscus at the mercury intrusion front [45]. The mercury size distribution (MIP-PSD) is obtained by linking the volume of intruding mercury with the corresponding pressures (and radii, respectively). It is well

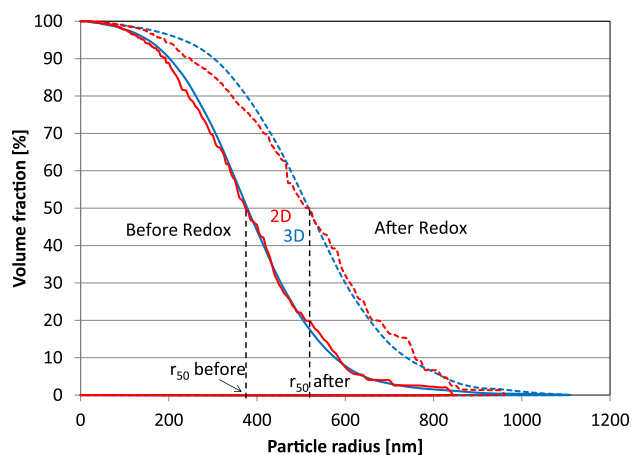


**Fig. 4.** Continuous particle size distributions (c-PSD) for the nickel-phase in SOFC anodes. The differences in the c-PSD curves before (solid lines) and after redox cycling (dashed lines) illustrate significant grain growth of the Ni-phase. 2D- and 3D-analyses reveal nearly identical results.

understood nowadays that the MIP method does not reveal the dimensions of the pore bulges because it is affected by the so-called ‘inkbottle effect’ [46]. Thereby the narrow bottlenecks hinder the intrusion of mercury unless a relatively high pressure is applied. At the so-called break-through pressure, mercury can pass many of the small bottlenecks at once and hence a large volume of the pores is filled instantaneously when this pressure is reached. Instead of measuring the dimensions of the pore bulges, the method thus reveals the dimensions of the bottlenecks. Consequently, the MIP-PSD curves are often characterized by a discontinuous shape with a steep increase of the volume within a small interval of radii that corresponds to the break-through event. Fig. 5 shows a comparison of the discontinuous MIP-PSD curves with the more continuous c-PSD curves for porous SOFC anodes. In contrast to the  $r_{50}$  value of the c-PSD, which gives the average size of the bulges, we interpret the  $r_{50}$  value of the MIP-PSD curves as a statistical measure for the average size of the bottlenecks. As will be discussed below, c-PSD and MIP-PSD provide complementary information and both together are required for the determination of the so-called constriction factor.

So far we have discussed mercury intrusion porosimetry as a physical experiment. In our study we simulate mercury intrusion based on microstructure information from tomography with a method described in Ref. [28]. For the MIP-simulation the same distance maps are used as for the c-PSD measurements. In contrast to c-PSD, additional constraints are introduced for the MIP simulation, which are linked to the simulation of an intrusion process. Thereby a new pixel is only allowed to join a region if it meets the growing criteria (i.e. connectivity- and radius-criteria). Practically, for radii smaller than the characteristic bottlenecks the growing criteria are fulfilled for a large number of voxels, which leads to a break through event with the observed discontinuous shape of the MIP-PSD curve.

Both methods (continuous-PSD and simulation of MIP) are based on the same distance maps, which assure a conceptual consistency in the perception of microstructural features. Nevertheless, two main differences exist between the two methods which are introduced by the constraints for region growing in the MIP simulation: a) The MIP-PSD is dominated by the inkbottle effect and it therefore reveals the dimensions of bottlenecks, in contrast to c-PSD which reveals the dimensions of the bulges. b) With c-PSD the entire volume of the phase is measured. In contrast, mercury intrusion only measures the volume of the interconnected regions. By comparing c-PSD and MIP-PSD the phase volume fractions, which are percolating and those, which are disconnected can be distinguished. In this way a percolation factor ( $P$ ) can be obtained. The phase volume fraction ( $\phi$ ) multiplied by the percolation factor ( $P$ ) gives the phase volume fraction, which is connected in a single percolating network.

In a previous study [20] we have investigated to what extent the selection of different intrusion areas and the variation of the associated intrusion direction will affect the results from MIP simulation. It turns out that the method provides highly reproducible results, which are nearly independent from the intrusion direction. Even for a non-homogeneous sample that shows a gradient in the phase volume fractions from one side to the other, the variation of the  $r_{50}$  values measured with six different intrusion directions was less than 2%. An important condition for such reliable and reproducible results is that the sample thickness exceeds the so-called critical intrusion depth, which is described in the next section.

### 2.3.4. Constriction factor ( $\beta$ )

In the literature it is often discussed that varying cross-sections along the transport pathways must have a strong impact on the

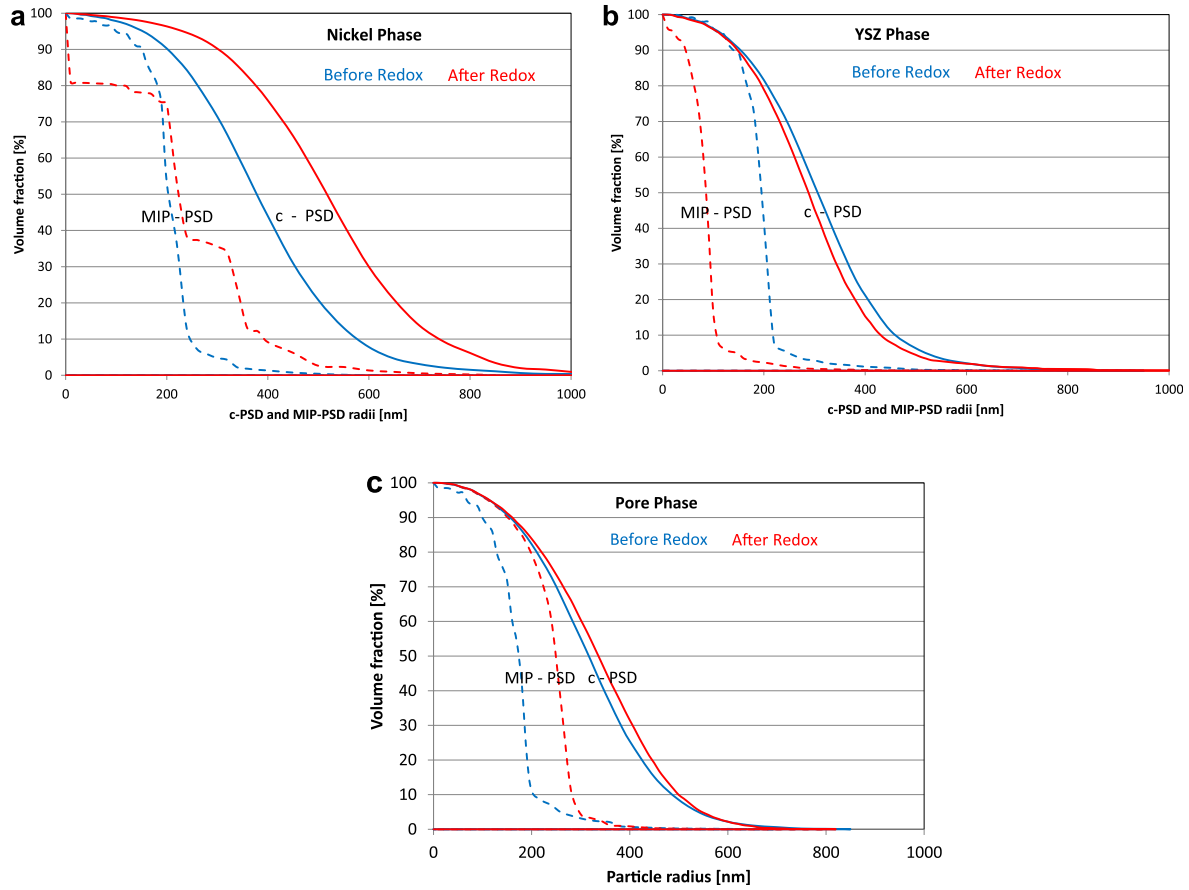


**Fig. 5.** Comparison of c-PSD (solid lines) vs. MIP-PSD (dashed lines) before and after redox cycling: The c-PSD curves mainly reflect the size of the bulges, whereas MIP-PSD reveals the size of the bottlenecks. Top: Coarsening of the Ni-phase during redox cycling is illustrated by the change of the c-PSDs. The dimensions of bottlenecks (MIP-PSDs) in nickel do not change significantly. Middle: In YSZ the bottlenecks are becoming larger during redox cycling (see change of MIP-PSDs), whereas the bulges remain constant (see c-PSDs). Bottom: Also in the pores, the size of the bulges remains constant. However, the bottlenecks increase during redox exposure as indicated by MIP-PSD.

effective transport properties [16–19]. In order to describe this effect a parameter called constriction factor ( $\beta$ ) was introduced by Petersen [27]. Petersen solved transport equations for cylinders with hyperbolic constrictions and studied the influence of different geometric parameters (e.g. angle of constriction, distance between constrictions, cross-sectional areas). He showed that the effective transport properties are mainly controlled by the constriction factor ( $\beta$ ), which for cylindrical systems is defined as the ratio of the cross-sectional areas at the bottlenecks ( $A_{\min}$ ) and bulges ( $A_{\max}$ ):

$$\beta = A_{\min}/A_{\max} = (\pi r_{\min}^2)/(\pi r_{\max}^2) = (r_{\min}/r_{\max})^2 \quad (3)$$

In tubes with constant radius the constriction factor has a value of 1. In networks with variable radius the constriction factor is  $<1$ . In a simplified way, the constriction factor can be interpreted as a parameter, which describes the effective phase volume fraction that contributes to transport. By multiplying the total phase volume fraction ( $\phi$ ) with the constriction factor ( $\beta$ ) one obtains the phase volume of a percolating network with pipes of a constant radius. Thereby the constant radius corresponds to the characteristic size of the bottlenecks (from MIP simulations). The constriction factor can thus be interpreted as a volume averaged parameter, which corrects for the portion of phase volume, which does not contribute to transport ('dead ends').

It must be emphasized that the shape of bottlenecks in real disordered microstructures may deviate considerably from a hyperbolic geometry. However, we are unable to quantify the

difference, which arises from the idealized description of a hyperbolic geometry compared to the real ones. Nevertheless, even in recent studies such as the modeling approach by Nelson et al. [18] (mentioned in the Introduction) the constrictions are described as idealized, centrisymmetrical geometries. More realistic descriptions are of course obtained, when the microstructures are described empirically based on high-resolution tomography. In our approach, the values for  $r_{\min}$  and  $r_{\max}$  are derived from 3D analysis of real microstructures and in this way the constrictivity obtained from equation (3) is not restricted to a hyperbolic case. Thereby the radius at the bottlenecks ( $r_{\min}$ ) is measured by (simulation of) mercury intrusion porosimetry (i.e. the  $r_{50}$  from MIP-PSD is considered to represent the  $r_{\min}$ ). In a similar way the radius at the bulges ( $r_{\max}$ ) is determined by means of the continuous PSD (i.e. the  $r_{50}$  from c-PSD is taken as  $r_{\max}$ ). The methodology for measuring the constriction factor was tested with respect to its reproducibility, reliability and sensitivity toward the influence from local heterogeneities in the microstructure (e.g. influence of single large pores or cracks on the corresponding  $r_{\min}$ ,  $r_{\max}$  and  $\beta$  was investigated) [20]. It was shown that the MIP-simulation provides reliable and reproducible results for the bottleneck dimensions under the condition that the thickness of the image volume exceeds the so-called 'critical intrusion depth'. It was found that the critical intrusion depth is approximately 2–5 times the size of the largest object (pore or particle, respectively). Below this thickness not all transport pathways have passed a narrow bottleneck, which is otherwise a characteristic constriction for transport over longer

distances. Hence 3D image windows of representative size are the main constraint for a reliable measurement of the constriction factor (and MIP-PSD, respectively).

The constriction factor was also measured by Wiedenmann et al. [21], who investigated transport properties of porous membranes for electrolysis cells. Thereby the effective ionic diffusivity was measured with impedance spectroscopy. It was shown for two different materials (olivine and wollastonite) that the effective ionic diffusivity ( $D_{\text{eff}}$ ) is mainly controlled by variations of the pore volume fractions ( $\phi_{\text{pore}}$ ) and the constriction factor ( $\beta$ ), whereas tortuosity was hardly affecting the transport properties of the investigated membranes.

### 2.3.5. Skeletonization, graph analysis and geometric tortuosity

Tortuosity ( $\tau$ ) describes the variations in the length of the transport pathways, and it was often considered as the main microstructural parameter, which controls transport properties in porous media [22,23,47]. However, until recently it was not possible to measure tortuosity directly from image data. Therefore the tortuosity was usually determined indirectly by means of physical experiments. Many different definitions are discussed in literature for the experimentally derived tortuosities. A thorough discussion and an overview of the different types of tortuosity are given by Clennell [25].

In the present study we focus on the direct measurement of tortuosity. New image analysis techniques nowadays enable the measurement of the so-called geometric tortuosity directly from tomography (see e.g. [48]). Thereby the lengths of the transport pathways are described statistically. For this purpose the segmented phase is first transformed into a skeleton. This step is done with Avizo software. The voxel-based skeleton is then further reduced into a graph, which mainly consists of branch vectors and node coordinates. The graph also contains the information of the effective branch lengths and the connectivity of branches at each node. For the calculation of the geometric tortuosity the so-called shortest pathways between each couple of inlet and outlet nodes are identified [49]. A statistical distribution of tortuosities is then obtained by measuring the lengths of all shortest pathways between the inlet and outlet couples in transport direction. Further details of our tortuosity analysis are given in previous publications from Keller et al. [29,30].

It must be emphasized that the indirectly determined experimental tortuosity is usually significantly higher than the geometric tortuosity, which is derived directly from the tomographs. In this context it should be noted that the experimental studies on transport and tortuosity usually also do not consider the constriction-effect. Consequently, the experimental tortuosity can be considered as a combination of the constriction-effect (i.e. bottlenecks) with the tortuosity-effect (i.e. variation of paths lengths). This may be the reason for the unrealistically high values that are measured for the experimental tortuosities. In our study we strictly distinguish between the effects of variable paths lengths and variable bottlenecks by measuring both, the geometric tortuosity and the constriction factor. We consider these parameters as the key information, which is needed to understand the microstructure degradation upon redox cycling and its influence on the effective transport properties of SOFC anodes (i.e. gas permeability, electric conductivity, ionic diffusivity).

### 2.4. Finite element modeling for calculation of effective transport properties

Finite Element (FE) modeling is performed based on grid representations of the phases in the cermet anodes. The procedure includes the following steps: a) Mesh generation based on microstructures from FIB-tomography. b) FE-simulation using SESES,

which is an in-house code for multi-physics simulation developed at Zurich University of Applied Sciences (ZHAW) (<http://www.zhaw.ch/engineering/icp/software/nm-seses.html>). c) Post-processing of FE-results for 3D-visualization (e.g. fluxes, stream-lines, concentrations, pressures and potential gradients).

- For mesh generation a cubic sub-volume of 12  $\mu\text{m}$  edge length is cropped from the segmented FIB-cubes (30 nm voxel size) for both samples (before and after redox). In a first step the triangulated surface is generated with Avizo software for each segmented phase. Thereby we apply the Avizo simplification editor, which makes use of some automated processes to improve the quality of the surface mesh. Then the surfaces are transformed into volumetric grids, which consist of approximately  $3 \cdot 10^6$  tetrahedrons for each phase.
- The effective transport properties of the electronic (Ni) and ionic (YSZ) conducting phases are evaluated in SESES by applying an external potential difference and by solving for the resulting current densities via ohms law. For the effective gas permeability and gas diffusivity in the pores the same equations can be applied but with pressure or concentration differences as driving forces instead of the electrical potential. The FE-simulation thus provides the effective transport properties such as electrical conductivity ( $\sigma_{\text{eff}}$ ) and from this result the corresponding  $M$ -factor of a specific microstructure can be determined according to equation (1) ( $M = \sigma_{\text{eff}}/\sigma_0$ ). It is the aim of the present project to compare the  $M$ -factors from the FE-simulation with the  $M$ -factors that are calculated based on directly measured microstructure parameters from tomography and image analysis (equation (2)). The comparison is considered as a reliability test for both methodologies.
- The FE-simulation also provides the local potentials and the flow or flux of the simulated transport species (e.g. electrons). For 3D-visualization these results are processed with Avizo, as illustrated in Fig. 13.

## 3. Results and discussion

### 3.1. Composition/volume fractions

In Fig. 3 compositions analyzed from 2D- and 3D-images are compared with each other. It should be noted that the 2D data are averaged from 2 FIB-cross-sections which were collected at different sample locations than the 3D-stacks with FIB-tomography. This is considered as a test for representativeness and reproducibility. For the pristine anode before redox cycling the results are: Nickel 30 vol% (2D)/32% (3D), YSZ 41 vol% (2D)/43% (3D) and pores 26% (2D)/29% (3D). Hence, the volume fractions analyzed from 2D cross sections and from FIB-tomography give very similar results, which confirms the methodic reliability. Fig. 3 also shows the compositions of degraded anodes. Redox cycling leads to a pronounced increase of porosity from <30% to 47%. As a consequence the solid contents decrease from 31 to 21 (+/–1)% (Ni) and from 42 to 32 (+/–1)% (YSZ), respectively. However, the solid volume fractions (i.e. Ni/(Ni + YSZ)) remain nearly constant at 42 (+/–1)% before and 39 (+/–2)% after redox cycling. Hence, the apparent compositional changes upon redox cycling are mainly due to an increase of porosity. The microstructure analyses indicate that volatilization of Ni is negligible (within analytical errors).

### 3.2. Continuous phase size distributions (c-PSD) vs. mercury intrusion simulation (MIP-PSD)

Fig. 4 shows a comparison of c-PSD curves for the nickel phase before and after redox cycling. The shift from solid (before) to



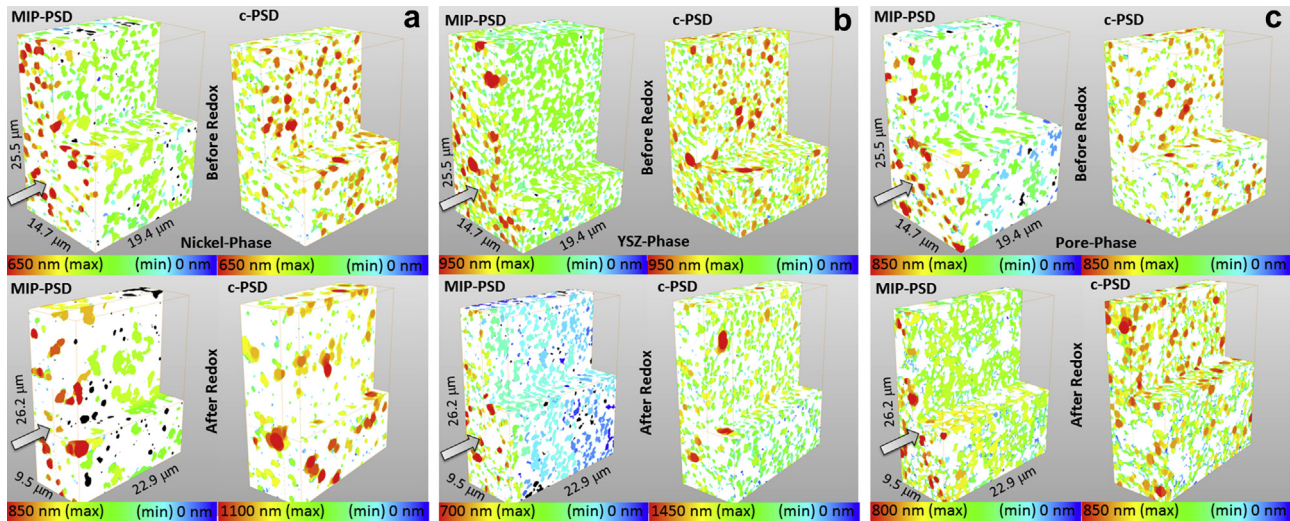


**Fig. 6.** a: Visualization of 3D-distance maps related to MIP-PSD (left) and c-PSD (right) for the Nickel-phase before (top) and after (bottom) redox cycling. The color code reflects the local particle radius (which also depends on the applied method). Note that the max radius in the color codes before and after redox is not the same (i.e. red is 650 nm before and 850/1100 nm after redox). For the MIP-simulation the intrusion direction (see arrow) is from left (current collector) to right (electrolyte). The MIP radii decrease along the transport pathways (left to right) due to the bottleneck effect. However the average size in MIP-PSD does not change significantly during redox cycling, which means that the dimensions of the bottlenecks remain stable (compare MIP-PSD curves in Fig. 5a). In contrast the size of the particle-bulges, which is reflected by the c-PSDs increases significantly during redox cycling (i.e. Ni-coarsening). In addition, the black domains in the MIP-PSD maps represent isolated particles, which increase during redox cycling. Redox cycling thus leads to a loss of percolation in the Ni-phase. b: Visualization of 3D-distance maps related to MIP-PSD (left) and c-PSD (right) for the YSZ-phase before (top) and after (bottom) redox cycling. Note that the MIP-radii decrease significantly after redox cycling, which is illustrated by the blue color (i.e. radii in the 10-nm range). In contrast the particle sizes in the c-PSD distance maps are nearly identical before and after redox cycling. Note that the percolation in YSZ is high also after redox cycling (i.e. only a few black domains appear in the MIP distance map after redox cycling). c: Visualization of 3D-distance maps related to MIP-PSD (left) and c-PSD (right) for the pores before (top) and after (bottom) redox cycling. As shown in Fig. 3 the pore volume increases during redox cycling. The difference of the MIP distance maps illustrates that the dimensions of the bottleneck in the pore network are increasing during redox cycling. The percolation of the pore phase remains ideal (no black disconnected domains). The c-PSDs are nearly identical before and after redox cycling, which indicates that the size of the pore bulges does not change upon redox cycling and pore swelling. (For interpretation of the references to colour in this figure legend, the reader is referred to the web version of this article.)

dashed lines (after redox) documents the increase of the nickel grain size. The  $r_{50}$  values increase from 375 to 520 nm. Fig. 4 also documents that the results from 2D- and 3D-analyses are nearly identical. A similar consistency between 2D- and 3D-analyses is also obtained for the other phases (Pores and YSZ, not shown in Fig. 4). Under the view of this consistency and for the sake of simplification only results from 3D analyses will be presented in the subsequent discussion of c-PSD and MIP-PSD analyses.

As shown in Fig. 5 for Ni (top), YSZ (middle) and pore (bottom), the MIP-PSDs always reveal smaller radii than the corresponding c-PSDs from the same microstructure. For the interpretations of the following figures it should be kept in mind that the dimensions of the bulges (particles and pores) are measured with c-PSD and the dimensions of the bottlenecks with MIP-PSD.

The c-PSD curves in Fig. 5a document the coarsening of Ni upon redox cycling whereby the  $r_{50}$  values increase significantly from 375 nm to 520 nm. In contrast the  $r_{50}$  values from the MIP-PSDs of nickel do hardly change, which indicates that the dimensions of the bottlenecks remain constant. The MIP-PSD curve for nickel after redox cycling has a step-like shape. Two steps at radii of approximately 370 and 250 nm indicate that two distinct break-through events occurred in the simulation. The third step at 0 nm (from 80 to 100% cumulative volume) indicates that 20% of the phase volume is not connected with the rest of the nickel phase. Hence the percolation factor of nickel decreases from 0.99 (before) to 0.8 (after redox cycling). Overall it can be assumed that the first two steps would be smoothed out if the MIP simulation were performed on the basis of a larger data volume. However the third step, which represents isolated nickel particles, is considered as a representative feature of the microstructure. Isolated nickel particles, which are randomly distributed throughout the microstructure, are also documented by FIB-tomography in Fig. 6a.

For YSZ the degradation is very different from the one in nickel. The c-PSDs of YSZ before and after redox cycling are almost identical. However, the  $r_{50}$  values from the MIP-PSDs decrease from 190 nm to 85 nm. Hence in YSZ the size of the particle bulges remains constant but the bottlenecks decrease by more than a factor of 2. This change leads to a strong limitation for the ionic transport in the anode.

Also for the pores the c-PSDs before and after redox are nearly identical and the MIP-PSDs are changing. However in contrast to YSZ, the bottlenecks in the pores are increasing during redox degradation. Hence, the redox cycling and associated swelling do not lead to larger pore bulges, but to a larger size of the bottlenecks, which improves gas diffusion in the anode.

The different perceptions of 'size distributions' become apparent when comparing the 3D-distance maps coming from analysis of MIP-PSD and c-PSD. For the nickel phase the c-PSD distance map after redox cycling (Fig. 6a, bottom-right) indicates much coarser grain size than before redox (top-right). Note the different scale bars for the color codes: before redox the red color reflects radii of 650 nm, after redox the red color reflects radii of 1100 nm. The distance map from MIP-PSD shows similar bottleneck dimensions before (Fig. 6a top-left) and after redox cycling (bottom-left). At the phase entrance (i.e. at the front face of cube) the pathways are not yet constricted (red colored). However at percolation depths longer than the critical intrusion distance the MIP maps reflect the dimensions of the characteristic bottlenecks, which are shown by the green color that corresponds to approximately 200 nm. The black domains which appear after redox cycling (bottom left), represent isolated islands of nickel. These black domains document a loss of percolation from 0.99 to 0.8 upon redox cycling. For YSZ (Fig. 6b) and for the pores (Fig. 6c) the degradation phenomena are mainly visible in the distance maps for

MIP-PSDs (left). Upon redox cycling the dimensions of bottlenecks become smaller in YSZ and larger in the pores.

### 3.3. Constriction factor ( $\beta$ )

Petersen [27] showed that for the determination of the constriction factor ( $\beta$ ) it is necessary to know the size of the bottlenecks (i.e.  $r_{\min}$ ) and the size of the bulges (i.e.  $r_{\max}$ ). These parameters can now be extracted from tomographs based on the recent improvements in 3D image analysis. Thereby the  $r_{50}$  from MIP is considered as a statistically meaningful value for the characteristic dimensions of the bottlenecks ( $r_{\min}$ ). In a similar way the  $r_{50}$  from c-PSD characterizes the average dimensions of the bulges ( $r_{\max}$ ). Hence, based on the MIP- and c-PSD analyses the constriction factor can now be determined for all three phases (Ni, YSZ, pores). These obtained values are summarized in Fig. 7 for the two anodes before and after redox cycling. The measurements illustrate that the constriction factor in the nickel phase ( $\beta_{\text{Ni}}$ ) decreases from 0.29 to 0.19 because nickel agglomeration leads to larger bulges. Surprisingly the dimensions of the bottlenecks in the nickel phase remain nearly constant.

In the 'rigid' YSZ phase the size of the particle bulges remains constant, whereas the dimensions of the bottlenecks decrease during redox cycling. This morphological change leads to a significant reduction of the constriction factor (i.e.  $\beta_{\text{YSZ}}$  changes from 0.4 to 0.09) for which the following mechanism can be assumed: The volume expansion due to nickel oxidation and the associated swelling of the anode leads to larger distances between the YSZ particles. Thereby the size of the rigid bulges remains constant. The bottlenecks represent weak locations in the rigid framework, which undergo thinning due to the overall dilation. The decrease of the bottleneck dimensions and associated decrease of the constriction factor have a negative impact on the ionic diffusivity (as documented experimentally [32]) and on the (thermo-) mechanical properties of the anode layer. At this stage there is no direct evidence that leads to a conclusive description of the mechanism, which could explain the measured thinning of the bottleneck dimensions in YSZ. Three different scenarios are possible: a) As suggested in literature [15,37,38], Zr-species may become mobile

under the anode operating conditions. However, the question is then why the material would be removed preferentially from the bottlenecks. b) Stress induced by the overall volume expansion may lead to a plastic deformation, which is localized mainly at the weak locations in the YSZ network (i.e. at the bottlenecks). c) The deformation at the bottlenecks may be brittle (instead of plastic), leading to the formation of numerous micro cracks. The associated dislocations and crack openings may be in the range a few nm only, so that these cracks are beyond imaging resolution. In fact, it is observed during sample preparation, that the microstructure in Ni–YSZ anodes after redox cycling is strongly weakened. YSZ particles tend to be ripped out from the sample surface during mechanical grinding and polishing. This may be taken as evidence for mechanical weakening of the YSZ structure, may be due to the formation of tiny cracks at the bottlenecks.

Also in the pores the dimensions of the bulges remain constant, which is surprising under the view of the ongoing swelling and associated increase of porosity. However the bottlenecks become larger and therefore the constriction factor increases from 0.3 to 0.5. Redox cycling thus leads to an improvement of the effective gas diffusivity and permeability in the pore network. This finding may be of importance for anode-supported systems where pathways for gas transport through the porous cermet layers are relatively long which may lead to losses from gas diffusion.

### 3.4. Tortuosity ( $\tau$ )

Tortuosity is determined by measuring statistically the length of the pathways in transport direction through the sample. The pathways are represented with a skeletonized network. For the Ni–YSZ anode after redox cycling the skeletons of all three phases are visualized in Fig. 8. Transport direction is  $x$  (i.e. the electrolyte was located to the left of the FIB cube, and the current collector/gas channels to the right). The nickel skeleton shows a heterogeneous structure on the length scale, which is captured by FIB-tomography (i.e.  $x \approx 10 \mu\text{m}$ ). In some 'centers' the number of branches is enriched. In between these 'centers' the number of connections is relatively low. This heterogeneous structure, which is only observed in the sample exposed to redox cycling, is attributed to the agglomeration of nickel. As shown in Fig. 8 the skeletons of the YSZ- and pore-phases are more homogeneous and dense also after the redox degradation.

The measured tortuosities are shown in Fig. 9 (statistical distributions) and in Fig. 10 (mean values). For the nickel phase the mean values of tortuosity hardly change (1.73 before/1.76 after), however the distribution becomes wider (std. dev. 0.11 before/0.21 after). Hence, although the visual impression indicates a strong change toward a more heterogeneous skeleton, the measured tortuosity of the nickel phase remains surprisingly constant.

For the YSZ phase the tortuosity increases from 1.55 to 2.13. As discussed already in the context of the constriction factor, the YSZ phase undergoes important changes at the bottlenecks, which are not obvious from visual inspection of the tomographs. The tortuosity in the pores decreases from 2.12 to 1.6, which can be attributed to the swelling, whereby a higher phase volume fraction leads to more direct and shorter transport pathways. Overall it must be emphasized that the variations of the tortuosity values in all three phases are rather small (all values between 1.55 and 2.2) which is not sufficient to explain significant changes of the transport properties.

### 3.5. $M$ -factor calculated with parameters from image analysis (IA)

As discussed in the Introduction the influence of the microstructure on the effective transport properties is described by the

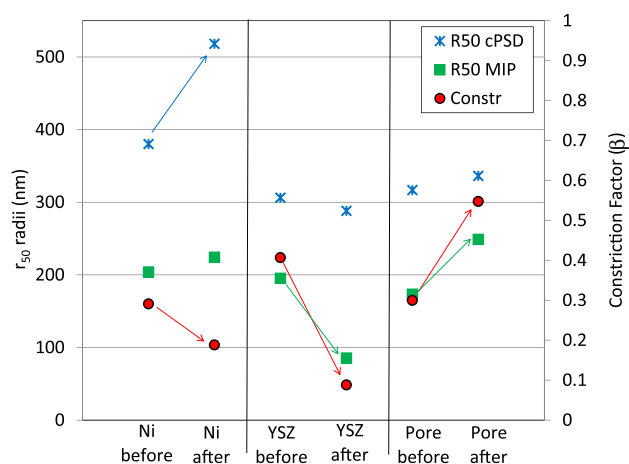


**Fig. 7.** Constriction factors (circles) for Ni, YSZ and pores before and after redox cycling. The constriction factors ( $\beta$ ) are calculated from the ratio  $(r_{\min}/r_{\max})^2 = \beta$ . Thereby  $r_{\min}$  is defined as the average size of the bottlenecks (i.e.  $r_{50}$  from MIP, shown as squares) and  $r_{\max}$  is defined as the average size of the bulges (i.e.  $r_{50}$  from c-PSD, shown as crosses). The constriction factor of nickel ( $\beta_{\text{Ni}}$ ) increases during redox cycling due to larger bulges (i.e. larger  $r_{50}$  c-PSD). In YSZ the bulges remain constant but the bottlenecks shrink (i.e. smaller  $r_{50}$  MIP). This morphological change also leads to a decrease of the constriction factor in YSZ ( $\beta_{\text{YSZ}}$ ). In the pores the bulges remain constant, but the bottlenecks expand which results in a higher constriction factor ( $\beta_{\text{Pore}}$ ).



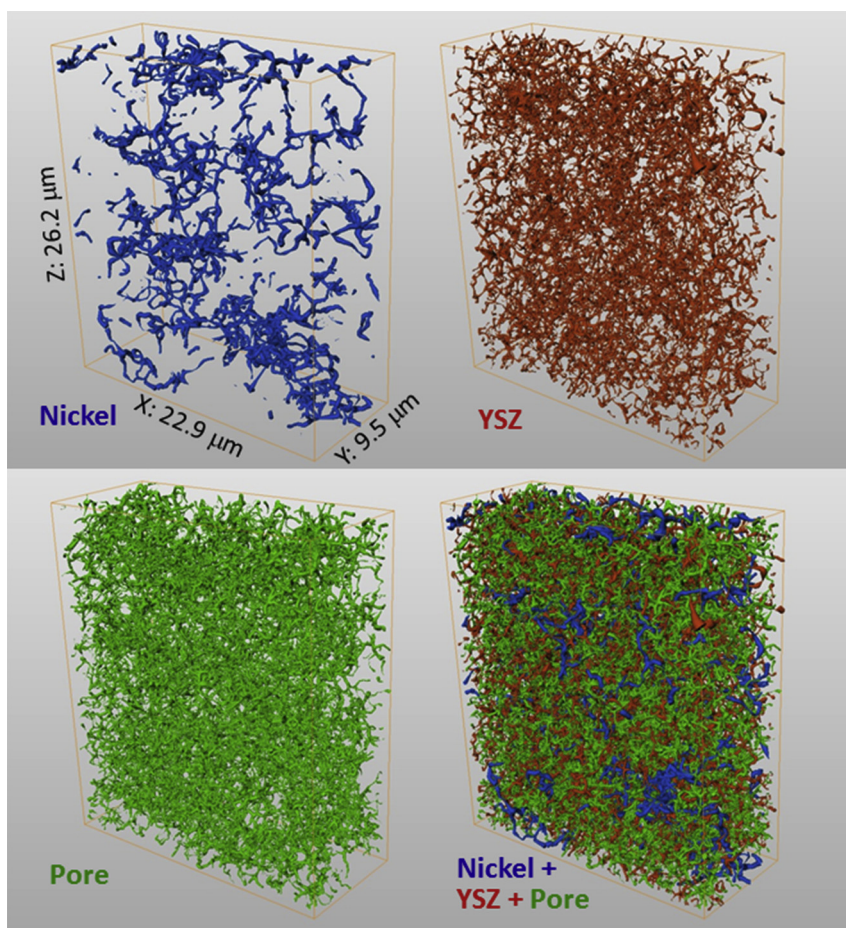


**Fig. 8.** Visualization of skeletonized phase networks in the anode sample after redox cycling for Ni (top left), YSZ (top right), pores (bottom left) and all three skeletons superimposed (bottom right). The network of nickel shows 'centers' with a relatively high density of branches. In between these centers the number of connections is low. This heterogeneous pattern is attributed to redox degradation and nickel agglomeration. The other two phases show uniform and dense skeleton networks. Note: Tortuosity is measured in  $x$ -direction. The electrolyte (not shown) is located to the left and the current collector to the right of the FIB-cubes.

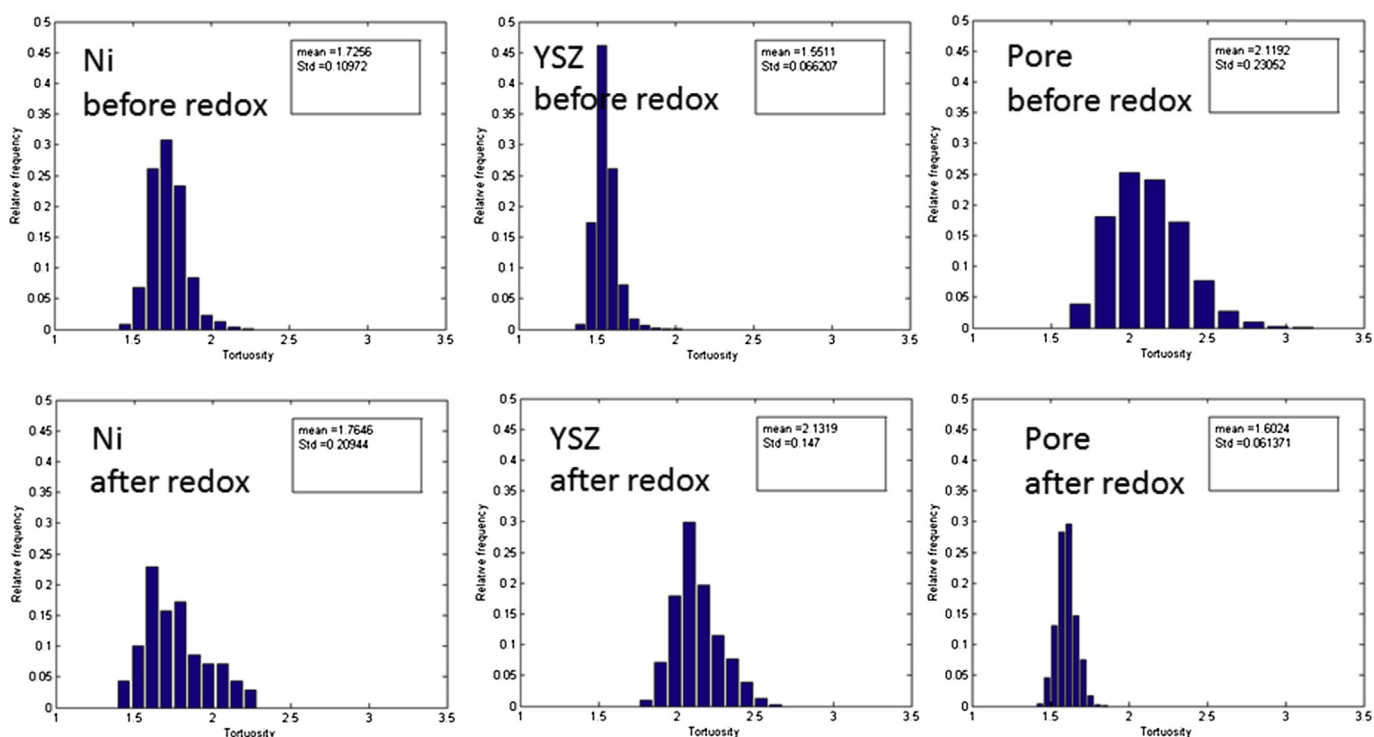


**Fig. 9.** Histograms of tortuosity for shortest pathways through the Ni-YSZ anodes (compare Fig. 8). Top row: before/bottom row: after redox cycling. Left: Ni/Middle: YSZ/Right: Pores. Tortuosity in the pores decreases, in YSZ it increases, whereas in Ni the average tortuosity remains constant. The mean values are summarized in Fig. 10.

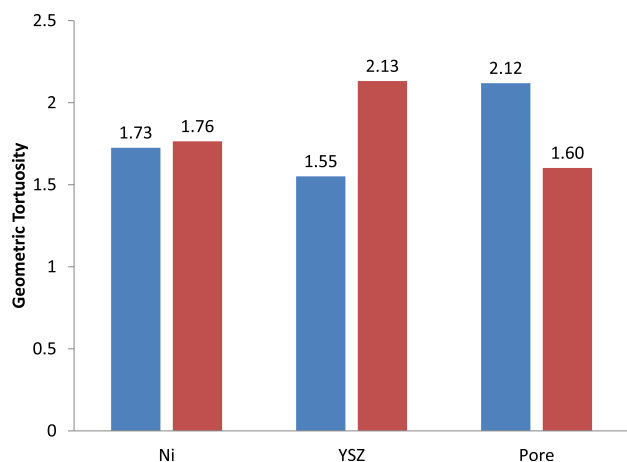


**Fig. 10.** Mean tortuosity for nickel, YSZ and pores before (left, hatched) and after (right, gray) redox cycling based on skeletonization and graph analysis of FIB-tomographs (see Fig. 8). Overall the variation is relatively small (1.55–2.13). During redox degradation tortuosity is increasing only in the YSZ phase, whereas in the nickel phase it remains constant and in the pores it decreases.

‘*M*-factor’. Based on the above reported results from quantitative image analysis (IA) the *M*-factor can now be calculated by using either eq. (2a) (with  $1/\tau$ ) or eq. (2b) (with  $1/\tau^2$ ). For the nickel phase the microstructure parameters are summarized in Fig. 11a and the corresponding 3D-visualizations of nickel are given in Fig. 12a. The *M*-factor of nickel calculated by eq. (2a) decreases from 0.05 to 0.02 during redox cycling which predicts that the electronic

conductivities in the anode samples are 5 and 2% respectively from the intrinsic conductivity in bulk nickel. When using eq. (2b) with  $1/\tau^2$  the resulting *M*-factors are divided by roughly a factor of 1.7. The most important change in the nickel microstructure is the loss of percolation (*P* reduces from 0.99 to 0.81) due to nickel agglomeration. After redox cycling 20% of the nickel volume forms small isolated grains, which is also visible in Fig. 12a (top right). In addition, the total volume fraction of nickel decreases from 0.32 to 0.22. As discussed earlier, this change is not attributed to volatilization of nickel since the ratio of Ni/(Ni + YSZ) remains constant. It is interpreted as a passive depletion due to overall volume expansion and macroscopic swelling of the anode layer. The third component which leads to a lower *M*-factor is change of the constriction factor. It decreases from 0.29 to 0.19, which is related to the grain growth of nickel ( $r_{\max}$ ), whereas the sizes of bottlenecks ( $r_{\min}$ ) remain constant. Although the microstructure of nickel undergoes significant reorganization this has little or no effect on the geometric tortuosity.

For YSZ the visual inspection of the FIB images before and after redox cycling shows only minor changes (Fig. 12b). The most obvious change is a passive depletion associated with macroscopic swelling (increase of porosity), which lowers the volume fraction of YSZ (from 42% to 31%). From a qualitative visualization it seems that the rigid ceramic phase is not affected by redox degradation. However, the *M*-factor of YSZ (see Fig. 11b) changes strongly from 0.11 to 0.01 (eq. (2a)) and from 0.07 to 0.006 (eq. (2b)), respectively. This significant drop is caused mainly by the reduction of the constriction factor from 0.41 to 0.09, which is attributed to the fact that the bottlenecks become thinner due to the overall volume expansion and dilation. Possible mechanisms of the thinning at the

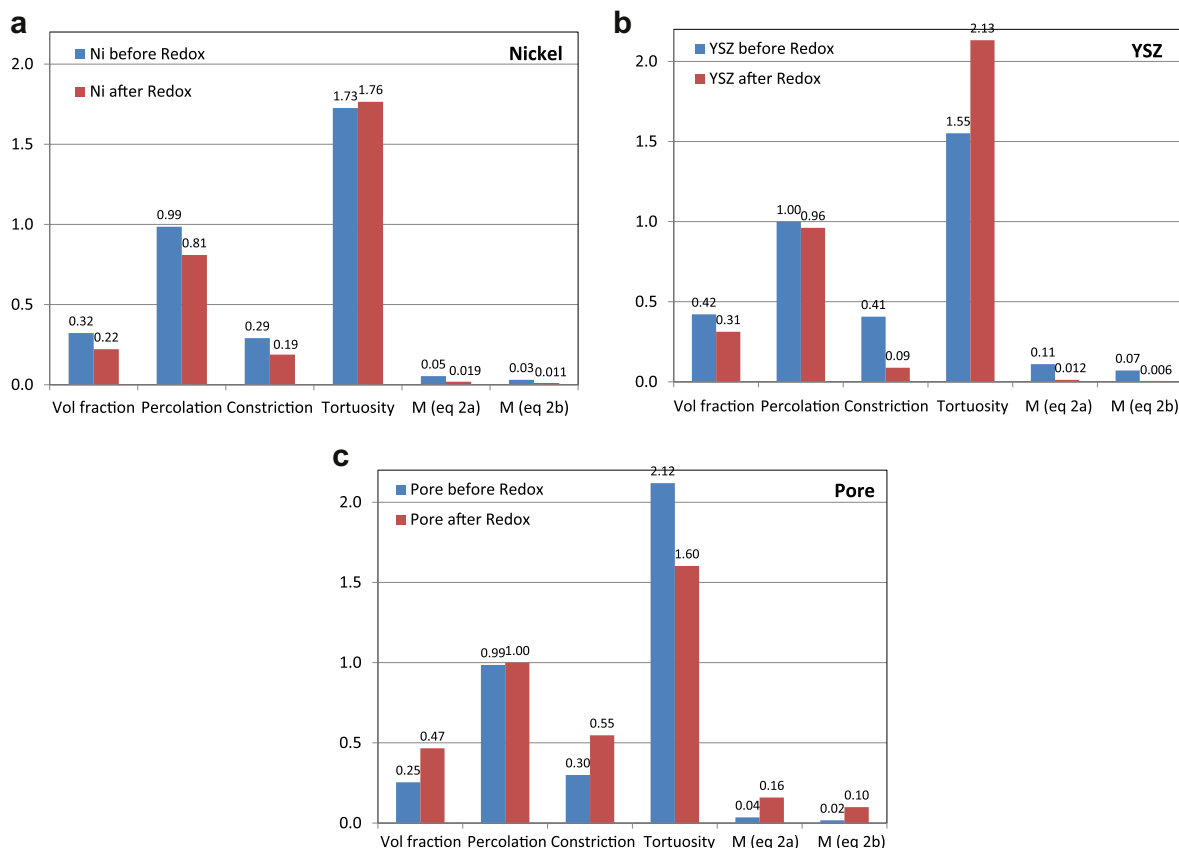


**Fig. 11.** Summary of microstructure parameters, which influence the transport properties and the *M*-factor. The twin bars reflect the values before (left) and after (right) redox cycling. According to equation (2a) and (2b) the *M*-factor can be calculated in two different ways (using either  $1/\tau$  or  $1/\tau^2$ ). For details see text. a = nickel/b = YSZ/c = Pores.



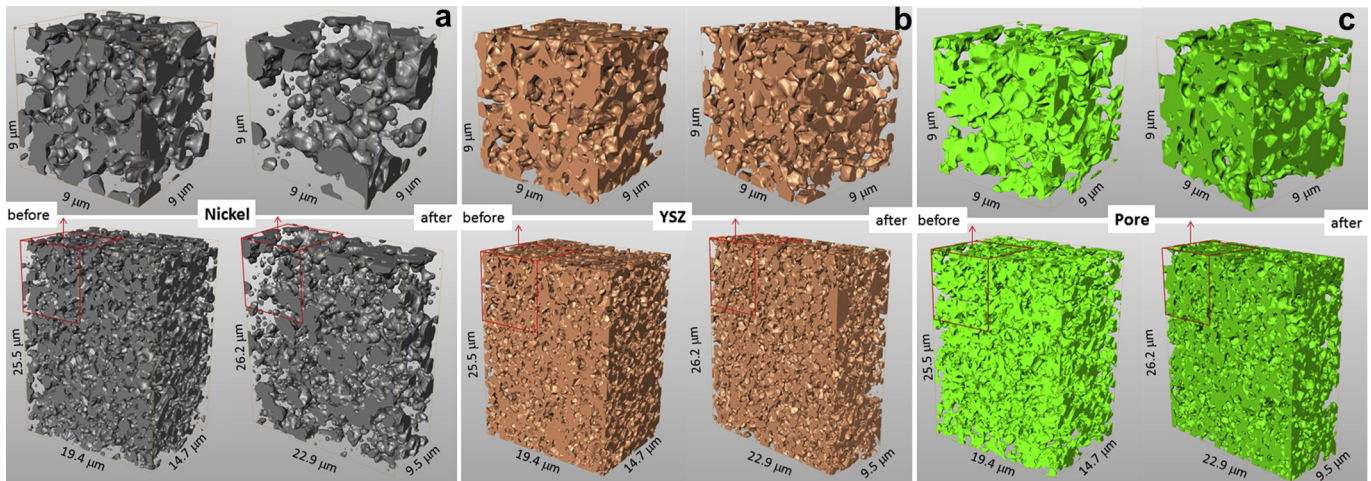


**Fig. 12.** 3D-visualization of nickel (a), YSZ (b) and pores (c). For each phase the left side represents the microstructure before redox cycling and the right side is after redox cycling. The most significant morphological changes for nickel (a) are grain coarsening, a decrease of the nickel volume fraction (passive depletion due to swelling) and the loss of percolation (formation of isolated particles). Also for YSZ (b) a decrease of volume fraction is visible (passive depletion due to swelling). The size of particle bulges remains nearly unchanged. Variations of the bottleneck dimensions are difficult to be seen. For the porosity (c) an increase of the volume fraction occurs during redox cycling and associated swelling. Changes of bottleneck dimensions and tortuosity are difficult to be seen by qualitative visualization.

constrictions were discussed previously in Section 2.3.4. Also changes of tortuosity and volume fraction contribute to the drop of the  $M$ -factor. The percolation factor remains close to 100% also after redox cycling. In summary, YSZ is usually considered as the rigid backbone, which gives stability to the composite anode. However the quantitative analyses indicate significant degradation that will reduce the ionic conductivity of the anode and most probably also mechanical stability.

The changes of the pore structure upon redox cycling are caused by expansion and swelling which leads to an increase of the  $M$ -factor from 0.04 to 0.16 (eq. (2a)) and from 0.02 to 0.1, (eq. (2b)), respectively. These results indicate that the effective gas diffusivity and permeability improve significantly. The pore volume fraction increases by nearly a factor of 2 from 0.25 to 0.47. The percolation factor stays at 100%. The constriction factor improves from 0.3 to 0.55 due to an increase of bottleneck dimensions. Also tortuosity improves from 2.12 to 1.6.

In summary many of the transport relevant features such as the bottleneck dimensions and tortuosity cannot be seen by qualitative visualizations such as Fig. 12. For a thorough investigation of microstructure effects quantitative image analysis combined with high resolution imaging is required. Nevertheless, up to this point it is still open whether the effect of tortuosity should be treated as  $1/\tau$  or as  $1/\tau^2$ .

### 3.6. Comparison of image analysis (IA) with finite element (FE)-modeling

In this section the results from finite element (FE) analysis are first discussed based on qualitative observations and then quantitatively, by comparing with the results from image analysis (IA). Transport simulations with the finite element method are performed on the basis of FIB-tomographs, which are transformed from voxel basis into a meshed grid. For each phase (Ni, YSZ, and pore) from the samples before and after redox cycling such a mesh is obtained. Fig. 13 illustrates phenomena related to the electrical current through the nickel phase (from left to right) as obtained from finite element (FE) modeling. Thereby locations with an abrupt change in color represent locally increased potential gradients (Fig. 13 top). Apparently the drop of potential is mainly triggered by narrow bottlenecks. In a similar way the color pattern of

the streamlines (Fig. 13 bottom) represents the local variation of fluxes and associated transport velocities. Again the locations with the highest transport velocities (i.e. the red sections of the streamlines) coincide with the locations of the narrow bottlenecks. Hence, visualization of electrical current and associated potential distributions from FE-simulation illustrates the important influence of narrow constrictions on the transport properties.

In Fig. 14 the  $M$ -factors from FE-analysis are compared with the  $M$ -factors that are obtained from direct measurement of microstructure parameters by image analysis (IA). The results obtained from FE-analysis confirm the trends, which are predicted by IA. In nickel and in YSZ the  $M$ -factors are strongly reduced after redox cycling. In contrast the  $M$ -factor increases in the pores. Hence for all three phases Finite Element (FE) analysis and image analysis (IA) show similar trends how the  $M$ -factors are affected by redox cycling. Nevertheless for some phases the  $M$ -factors from FE-analysis and from IA show substantially different  $M$ -factors (e.g. for YSZ before redox cycling). A possible reason for this difference is the uncertainty introduced by grid generation and meshing. It is assumed that for example minor changes in the bottleneck dimensions, which may result from mesh-generation, can have a strong impact on the results from FE-simulation. A thorough analysis of grid generation and associated mesh quality is beyond the scope of the present study but it is the issue of our ongoing research. Thereby the meshes used for FE-analysis will be transformed back to a voxel-based format and the topology parameters are then compared with the ones from the initial tomography data. Although there are some uncertainties regarding mesh quality at the present stage, the FE-analyses provide an independent estimation of  $M$ -factors in all three phases. And the comparison of both methods shows similar trends. Experimentally the  $M$ -factors are only available for the electronic conductivity in nickel.

### 3.7. Effective electronic conductivity of nickel: comparison of experiments, image analysis and FE-simulation

The samples of the present study are selected from a previous investigation on redox degradation. The corresponding experimental results published in Iwanschitz et al. [36] include impedance spectroscopy and conductivity measurements at 850 and 950 °C. In Fig. 15 the evolution of the measured in-plane

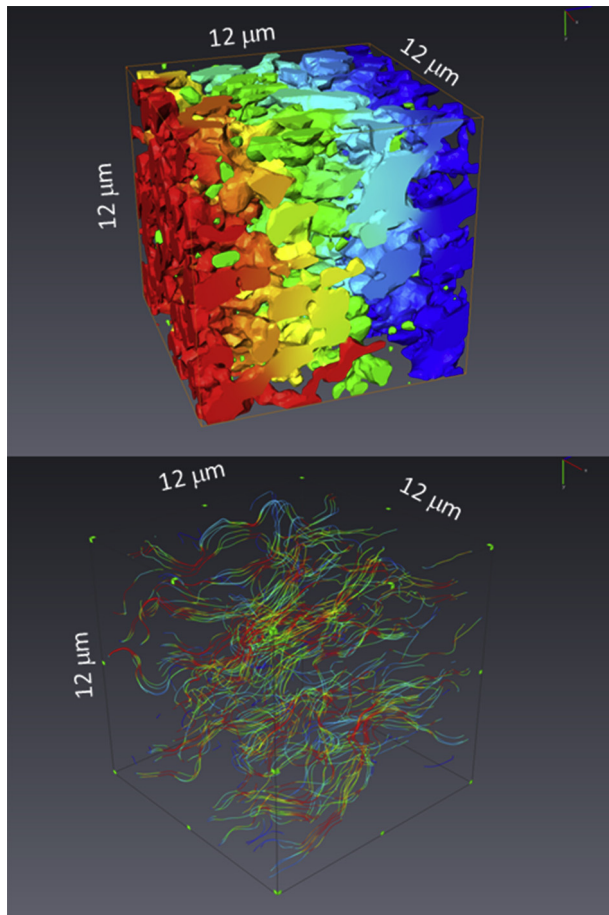


**Fig. 13.** Illustration of results from finite element modeling (FEM). The simulations are performed on a grid with  $10^6$  tetrahedrons, which is obtained by meshing of the segmented FIB data. Both images illustrate phenomena related to the electronic transport through the nickel phase in a cermet anode before redox cycling. Top: The color code represents the local drop of the (externally applied) potential (red = maximum potential, blue = minimum). Potential drop is calculated by solving for electronic current (from left to right) via ohm's law. The potential gradients are locally increased due to microstructure effects. Note the importance of bottlenecks. Bottom: Streamlines associated with electronic current in the nickel phase. The local velocities associated with the flux pattern are strongly increased at the bottlenecks (red = maximum velocity) and much slower at locations corresponding to large particles/bulges (blue = minimum velocity). (For interpretation of the references to colour in this figure legend, the reader is referred to the web version of this article.)

conductivity during redox degradation at 950 °C is redrawn. The effective conductivity first slightly increases (from 600 to 650 S/cm) and then gradually decreases to 200 S/cm after eight redox cycles.

For comparison with results from IA, the effective conductivities ( $\sigma_{\text{eff}}$ ) are calculated from the previously measured  $M$ -values according to equation (1), whereby an intrinsic conductivity ( $\sigma_0$ ) of  $2.21 \cdot 10^4$  S/cm is used for nickel at 950 °C. This intrinsic conductivity at 950 °C is calculated under the assumption of a linear temperature dependence as follows:  $\sigma_{0,950} = \sigma_{0,20} / (1 + 0.0059 \cdot (T_{950} - T_{20}))$ , where  $\sigma_{0,20}$  at 20 °C is  $1.43 \cdot 10^5$  S/cm [50]. For each of the two samples (before and after redox cycling) two different  $M$ -values were obtained, depending on which option in eq. (2a) ( $1/\tau$ ) or eq. (2b) ( $1/\tau^2$ ) was chosen. Overall the effective conductivities from image analysis calculated by eq. (2b) (rhombs in Fig. 15) match very well with the measured conductivities before and after 8 redox cycles. If eq. (2a) is used (squares in Fig. 15) then the calculated results are higher than the experimentally measured conductivities. This indicates that a better match is obtained when the effect of tortuosity is considered by  $1/\tau^2$ .

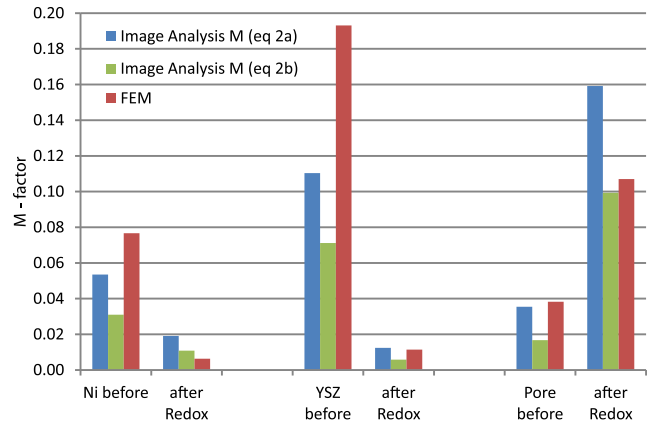


**Fig. 14.** Comparison of  $M$ -factors (for Ni, YSZ and pores), which are calculated based on microstructure parameters from image analysis (IA) and which are simulated with finite element modeling (FEM). The  $M$ -factors from image analysis are calculated in two different ways following eq. (2a) (with  $1/\tau$ ) and eq. (2b) (with  $1/\tau^2$ ). All results from IA and FEM indicate that redox cycling leads to lower  $M$ -factors for nickel and YSZ whereas the  $M$ -factor for the pores increases due to redox induced degradation.

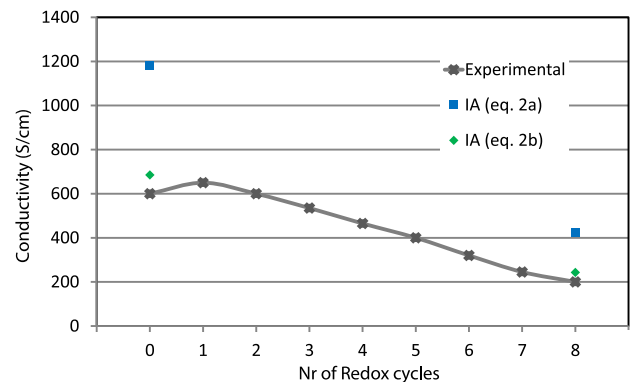


**Fig. 15.** Effective electrical conductivity in cermet anodes and its degradation upon redox cycling at 950 °C. The crosses represent experimental measurements (redrawn after Ref. [36]). The effective conductivities are calculated by substitution of the  $M$ -factors from Image analysis (IA) into equation (1). For this calculation an intrinsic conductivity of  $2.21 \cdot 10^4$  S/cm is assumed for nickel at 950 °C. The squares and the rhombs represent data points calculated from results of IA.

#### 4. Conclusions

In 'historical' papers between 1920 and 1980 [22–27] basic relationships between topological parameters and the effective transport properties were postulated based on theoretical and semi-empirical considerations (see equations (1) and (2)). For a very long time these postulated relationships could not be validated, because suitable techniques that are necessary for a quantitative description of the topological parameters were missing. With the recent progress in 3D-analysis all relevant parameters (constrictivity, tortuosity, percolation factor, volume fraction) can now be determined. The aim of this paper is thus to describe the new methodology for 3D analysis and to apply these methods for a first validation of the postulated relationship based on an example with SOFC cermet anodes. The present investigation was focused strongly on the development and description of a suitable 3D-methodology, which is expensive and time consuming. The study is thus limited to only one material that is tested before and after redox cycling. Based on these preliminary results it can be confirmed that the postulated equations capture the basic relationships between microstructure and effective transport

properties. However, in order to elaborate on the details of these relationships, the investigation must be extended to a broader experimental basis (work in progress).

3D image analysis (IA) thus enables a thorough quantitative description of the transport relevant parameters (i.e. constriction factor, percolation factor, tortuosity and phase volume fraction). The comparison of results from IA with experimental results indicates that the effect of tortuosity should be accounted for by  $1/\tau^2$ . By substitution of the mentioned parameters into equation (2b) the  $M$ -factor can be calculated, which enabled an accurate prediction of the effective transport properties in nickel before and after redox cycling. Hence, based on the analysis of these four parameters it can be determined which morphological features actually control the transport properties and how these features change upon redox cycling.

In the investigated anodes the  $M$ -factor (according to eq. (2b)) of nickel decreases from initially 3% to 1.2% after 8 redox cycles at 950 °C. The associated loss of electronic conductivity in the nickel phase is mainly due to a reduction of the percolation factor (i.e. formation of isolated domains) and a decrease of the constriction factor. In YSZ the  $M$ -factor changes significantly from 7% to 0.6%. The corresponding loss of ionic conductivity is mainly caused by a decrease of the constriction factor in YSZ. Thereby, the average size of the bottlenecks changes from 190 to 85 nm. Obviously, the overall volume expansion associated with Ni oxidation also leads to a dilation of the YSZ network, whereby strain is localized at the bottlenecks. Redox degradation induces an improvement of the gas diffusivity. Thereby the  $M$ -factor of the pores increases from 2% to 10% due to the overall swelling, which results in a higher pore volume fraction and a higher constriction factor.

The 3D data from FIB-tomography is also used as a basis for FE-simulation. For this purpose the tomographs are transformed into grid representations of the microstructure. FE-analysis predicts similar changes of the  $M$ -factors as the quantitative image analysis. For two simulations (i.e. Ni and YSZ before redox) the results deviate markedly from the ones obtained by IA. It is assumed that uncertainties are introduced by the mesh generation. The influence of different meshing procedures is currently analyzed in ongoing investigations.

The results from IA are also compared with experimental measurements. The electrical conductivities at 950 °C are characterized with four-point measurements. The experimentally measured conductivities (i.e. 600 S/cm before and 200 S/cm after 8 redox cycles) match well with the predictions from image analysis (i.e. 685 S/cm before and 243 S/cm after redox).

In the present study we focused on the effective transport properties and on how they are influenced by microstructure effects. In a forthcoming paper we will also present quantitative analyses for the electrochemically active reaction sites (i.e. triple phase boundaries, TPB). In addition the FE-model will be extended so that the transport processes are coupled with the electrochemical reactions. In this way a thorough description of the microstructure effects on the electrode performance will be obtained. This approach is considered as a basis for a better understanding of the electrode degradation mechanisms and for further optimization of the anode microstructures.

## Acknowledgments

The research presented in this paper was performed within the frameworks of a Swiss national project 'SOF-CH' (SFOE/BFE project No. SI 500'084) and a EU project 'SOFCH-life' (EU FP7/2007-2013, Fuel Cell and Hydrogen Joint Undertaking FCH-JU, project No. 256'885). The involved PhD-student (O. Pecho) was supported financially by SNF (Swiss National Science Foundation, Grant No. 200021\_135270). All financial supports are gratefully acknowledged.

## References

- [1] P. Costamagna, P. Costa, V. Antonucci, *Electrochimica Acta* 43 (1998) 375–394.
- [2] A. Abbaspour, J.-L. Luo, K. Nandakumar, *Electrochimica Acta* 55 (2010) 3944–3950.
- [3] A. Abbaspour, X. Wen, K. Nandakumar, J. Luo, K.T. Chuang, *Journal of Power Sources* 185 (2008) 961–966.
- [4] B. Kenney, M. Valdmann, C. Baker, J.G. Pharoah, K. Karan, *Journal of Power Sources* 189 (2009) 1051–1059.
- [5] L. Holzer, M. Cantoni, in: I. Utke, S.A. Moshkalev, P. Russell (Eds.), *Nanofabrication Using Focused Ion and Electron Beams: Principles and Applications*, Oxford University Press, New York, 2012, pp. 410–435.
- [6] J.R. Wilson, W. Kobsiriphat, R. Mendoza, H.-Y. Chen, J.M. Hillier, D.J. Miller, K. Thornton, P.W. Voorhees, S.B. Adler, S.A. Barnett, *Nature Materials* 5 (2006) 541–544.
- [7] P.R. Shearing, J. Golbert, R.J. Chater, N.P. Brandon, *Chemical Engineering Science* 64 (2009) 3928–3933.
- [8] P.R. Shearing, Q. Cai, J.I. Golbert, V. Yufit, C.S. Adjiman, N.P. Brandon, *Journal of Power Sources* 195 (2010) 4804–4810.
- [9] N. Vivet, S. Chapin, E. Estrade, T. Piquero, P.L. Pommier, D. Rochais, E. Bruneton, *Journal of Power Sources* 196 (2011) 7541–7549.
- [10] N. Shikazono, D. Kanno, K. Matsuzaki, H. Teshima, S. Sumino, N. Kasagi, *Journal of the Electrochemical Society* 157 (2010) B665–B672.
- [11] L. Holzer, M.B.B. Iwanschitz, M. Cantoni, T. Hocker, T. Graule, *Journal of Power Sources* 196 (2011) 7076–7089.
- [12] L. Holzer, B. Iwanschitz, T. Hocker, B. Münch, M. Prestat, D. Wiedenmann, U. Vogt, P. Holtappels, J. Sfeir, A. Mai, T. Graule, *Journal of Power Sources* 196 (2011) 1279–1294.
- [13] J.R. Izzo, A.S. Joshi, K.N. Grew, W.K.S. Chiu, A. Tkachuk, S.H. Wang, W. Yun, *Journal of the Electrochemical Society* 155 (2008) B504–B5408.
- [14] K.N. Grew, Y.S. Chu, J. Yi, A.A. Peracchio, J.R. Izzo, Y. Hwu, F. De Carlo, W.K.S. Chiu, *Journal of the Electrochemical Society* 157 (2010) B783–B792.
- [15] G.J. Nelson, K.N. Grew, J.R. Izzo, J.J. Lombardo, W.M. Harris, A. Faes, A. Hessler-Wyser, J. Van Herle, S. Wang, Y.S. Chu, A.V. Virkar, W.K.S. Chiu, *Acta Materialia* 60 (2012) 3491–3500.
- [16] K.N. Grew, A.A. Peracchio, A.S. Joshi, J.R. Izzo Jr., W.K.S. Chiu, *Journal of Power Sources* 195 (2010) 7930–7942.
- [17] K.N. Grew, A.A. Peracchio, W.K.S. Chiu, *Journal of Power Sources* 195 (2010) 7943–7958.
- [18] G.J. Nelson, A.A. Peracchio, W.K.S. Chiu, *Journal of Power Sources* 196 (2011) 4695–4704.
- [19] G.J. Nelson, B.N. Cassenti, A.A. Peracchio, W.K.S. Chiu, *Journal of Power Sources* 205 (2012) 48–56.
- [20] L. Holzer, D. Wiedenmann, B. Muench, L. Keller, M. Prestat, P. Gasser, I. Robertson, B. Grobety, *Journal of Materials Science* 48 (2013) 2934–2952.
- [21] D. Wiedenmann, L. Keller, L. Holzer, J. Stojadinovic, B. Münch, L. Suarez, B. Fumey, H. Hagendorfer, R. Brönnimann, P. Modregger, M. Gorbar, U.F. Vogt, A. Züttel, F. La Mantia, R. Wepf, B. Grobety, *AIChE Journal* 59 (2013) 1446–1457.
- [22] J. Kozeny, *Sitzungsberichte Akademie der Mathematischen- und Naturwissenschaften, Wien* 136a (1927) 271–306.
- [23] P.C. Carman, Butterworths, London, 1956, pp. 12–13.
- [24] G.E. Archie, *Transactions of AIME* 146 (1942) 54–61.
- [25] M.B. Clennell, in: M.A. Lovell, P.K. Harvey (Eds.), *Developments in Petrophysics*, Geological Society Special Publication, London, 1997, pp. 299–344.
- [26] J. Van Brakel, P.M. Heertjes, *International Journal of Heat and Mass Transfer* 17 (1974) 1093–1103.
- [27] E.E. Petersen, *AIChE Journal* 4 (1958) 343–345.
- [28] B. Münch, L. Holzer, *Journal of the American Ceramic Society* 91 (2008) 4059–4067.
- [29] L.M. Keller, L. Holzer, R. Wepf, P. Gasser, *Applied Clay Science* 52 (2011) 85–95.
- [30] L.M. Keller, L. Holzer, R. Wepf, P. Gasser, B. Münch, P. Marschall, *Physics and Chemistry of the Earth* 36 (2011) 1539–1544.
- [31] D. Sarantaridis, A. Atkinson, *Fuel Cells* 7 (2007) 246–258.
- [32] T. Klemens, M. Mogensen, *Journal of the American Ceramic Society* 90 (2007) 3582–3588.
- [33] A.V. Virkar, J. Chen, C.W. Tanner, J.W. Kim, *Solid State Ionics* 131 (2000) 189–198.
- [34] D. Fouquet, A.C. Muller, A. Weber, E. Ivers-Tiffée, *Ionics* 9 (2003) 103–108.
- [35] Q. Jeangros, A. Faes, J.B. Wagner, T.W. Hansen, U. Aschauer, J. Van Herle, A. Hessler-Wyser, R.E. Dunin-Borkowski, *Acta Materialia* 58 (2010) 4578–4589.
- [36] B. Iwanschitz, J. Sfeir, A. Mai, M. Schütze, *Journal of the Electrochemical Society* 157 (2010) B269–B278.
- [37] N. Balakrishnan, T. Takeuchi, K. Nomura, H. Kageyama, Y. Takeda, *Journal of the Electrochemical Society* 151 (2004) A1286–A1291.
- [38] M. Hattori, Y. Takeda, Y. Sakaki, A. Nakanishi, S. Ohara, K. Mukai, J.-H. Lee, T. Fukui, *Journal of Power Sources* 126 (2004) 2004.
- [39] L. Holzer, P. Gasser, A. Kaech, M. Wegmann, A. Zingg, R. Wepf, B. Muench, *Journal of Microscopy* 227 (2007) 216–228.
- [40] L. Holzer, F. Indutnyi, P. Gasser, B. Münch, M. Wegmann, *Journal of Microscopy* 216 (2004) 84–95.
- [41] L. Holzer, B. Münch, *Microscopy and Microanalysis* 15 (2009) 130–146.



- [42] L. Holzer, B. Münch, M. Wegmann, R. Flatt, P. Gasser, *Journal of the American Ceramic Society* 89 (2006) 2577–2585.
- [43] M.D. Uchic, L. Holzer, B.J. Inkson, E.L. Principe, P. Munroe, *MRS Bulletin* 32 (2007) 408–416.
- [44] L. Holzer, B. Muench, M. Rizzi, R. Wepf, P. Marschall, *Applied Clay Science* 47 (2010) 330–342.
- [45] E.W. Washburn, *Physical Review* 17 (1921) 273–283.
- [46] S. Diamond, *Cement and Concrete Research* 30 (2000) 1517–1525.
- [47] S.K. Bhatia, *Journal of Catalysis* 93 (1985) 192–196.
- [48] R. Thiedmann, C. Hartnig, I. Manke, V. Schmidt, W. Lehnert, *Journal of the Electrochemical Society* 156 (2009) B1339–B1347.
- [49] W.B. Lindquist, S.M. Lee, D.A. Coker, K.W. Jones, P. Spanne, *Journal of Geophysical Research* 101 (1996) 8297–8310.
- [50] D.R. Lide (Ed.), *CRC Handbook of Chemistry and Physics*, CRC Press.